Hindawi
Journal of Mathematics
Volume 2022, Article ID 3257808, 13 pages
https://doi.org/10.1155/2022/3257808

*Research Article*

# Implementing the Vieta–Lucas Collocation Optimization Method for MHD Casson and Williamson Model under the Effects of Heat Generation and Viscous Dissipation

**M.M. Khader**,[1,2] **A. Eid**,[3] **and M. Adel**[4]

[1]*Department of Mathematics and Statistics, College of Science, Imam Mohammad Ibn Saud Islamic University (IMSIU), Riyadh 11566, Saudi Arabia*
[2]*Department of Mathematics, Faculty of Science, Benha University, Benha, Egypt*
[3]*Department of Physics, College of Science, Imam Mohammad Ibn Saud Islamic University (IMSIU), Riyadh 11566, Saudi Arabia*
[4]*Department of Mathematics, Faculty of Science, Cairo University, Giza, Egypt,*

Correspondence should be addressed to M.M. Khader; mmkhader@imamu.edu.sa

Received 16 February 2022; Revised 24 March 2022; Accepted 29 March 2022; Published 14 May 2022

Academic Editor: M. M. Bhatti



Theoretical investigation of magnetohydrodynamics (MHD) Casson and Williamson fluid flow and heat and mass transfer in laminar flow through a stretching sheet in the presence of heat generation is carried out in this study. The convective wall temperature and convective wall mass boundary condition are taken into account in this study. A study is also provided, which looks into the impact of viscous dissipation. Except for a temperature-dependent thermal conductivity, all properties of the proposed model are assumed to be constants in the study. The spectral collocation method based on the shifted Vieta–Lucas polynomials is used to give an approximate formula for the $n$-order derivative and solve numerically the coupled momentum, energy, and mass equations. This method is used to convert the problem's system of ordinary differential equations (ODEs) into a nonlinear system of algebraic equations. This system is built as a restricted optimization problem and optimized to obtain the series solution's unknown coefficients. Some theorems are provided to investigate the method's convergence. The statistics, which are given visually, were compared to the results of other researchers' theoretical analysis.

## 1. Introduction

As an established fact, the bulk of fluids dealt with by engineers and scientists, such as air, water, and oils, can be considered Newtonian. However, in many circumstances, the assumption of Newtonian behavior is incorrect, and the non-Newtonian response must be modeled instead. Situations like this exist in the chemical and plastics processing industries. Non-Newtonian behavior is also obtained in the mining industry, where slurries and muds are frequently handled, as well as in lubricating and biomedical flow applications. As a result, simulation of non-Newtonian fluid flow phenomena is critical in the industry. In fluid dynamics, non-Newtonian Casson fluid flow in various physical situations has been the subject of extensive study due to its important application in industry and technology. Possibly the earliest formulation of the problem and analytical study was due to Casson [1] who, in 1959, postulated the problem of Casson fluid flow and heat transfer at a constant wall temperature. This model, sometimes, will be more appropriate, especially in rheological data than other models for many materials [2]. In this respect, more contributors in the field of laminar non-Newtonian Casson fluid flow and heat transfer are well-known and were recorded in [3–7]. Another important model is the Williamson model, which has particular advantages over other non-Newtonian models in which it can deal with fluids having minimum viscosity and fluids that have maximum viscosity. Williamson [8] was the pioneering researcher, and he proposed the foundations of this model and confirmed the obtained results

experimentally. The importance of this type of model was the motivation for more studies in this field [9–15]. In terms of physical characteristics, there exist non-Newtonian fluids that mix the Casson and Williamson models. Consequently, these fluids can be defined as a Casson–Williamson model, as shown in our research, which is based on prior Casson–Williamson model studies [16]. An interesting feature here is that we follow Abbas and Megahed [17] in their model. They used the Casson–Williamson fluid flow and heat mass transfer models over a nonuniform stretching surface in the presence of viscous dissipation and thermal radiation.

In fact, most nonlinear differential equations have no exact solutions, so numerical and approximate techniques are the semiunique way to solve these types of ODEs [18–24]. The spectral methods are one of the most useful tools for simulating differential equations (partial, fractional, and variable order). The most famous advantage of these methods is their capability to generate accurate outcomes with a very small degree of error of freedom. The orthogonality property of some important polynomials, such as Vieta–Lucas polynomials, is used to approximate functions in the interval $[a, b]$. These polynomials have a main and important role in these methods for ODEs [25].

Despite the importance of non-Newtonian behavior in modern technology and industry, no investigation of the Casson–Williamson model with viscous dissipation due to a nonuniform stretched sheet has been attempted thus far. As a result, an attempt is made in this study to use the Vieta–Lucas spectral collocation approach to get a numerical solution for the non-Newtonian Casson–Williamson model due to a nonuniform stretching sheet while accounting for the magnetic field, viscous dissipation, and heat generation.

## 2. Mathematical Analysis

In this section, we will look at a specific sort of non-Newtonian fluid that combines the Casson and Williamson types in terms of properties. This kind is known as the Casson–Williamson type, as previously mentioned in the literature study [16]. Similarly, the following relation can be used to express the stress tensor $\tau_{ij}$ of this type:

$$\tau_{ij} = \mu\left(\left(1+\frac{1}{\beta}\right)\frac{\partial u}{\partial y} + \frac{\Gamma}{\sqrt{2}}\left(\frac{\partial u}{\partial y}\right)^2\right), \tag{1}$$

where $\mu$ is the fluid viscosity, $\beta$ is the Casson parameter, and $\Gamma$ is the Williamson coefficient. So, herein, we consider the steady motion of an incompressible non-Newtonian Casson–Williamson fluid with an electrical conductivity $\sigma$ past a nonuniform stretching sheet. The fluid thermal conductivity is assumed to be a function of temperature. The Cartesian coordinate system is considered such that the $x$-axis is taken along the sheet in the direction of the motion and the $y$-axis is perpendicular to it. The sheet is maintained at a temperature $T_w$ and a concentration $C_w$ which are higher than $T_\infty$ and $C_\infty$, respectively, where $T_\infty$ and $C_\infty$ are the temperature and concentration of the fluid at the ambient. Heat generation mechanisms are also assumed to have an impact on the energy field. The $y$-direction magnetic field with a uniform strength of $B$ is assumed perpendicular for the flow region. Furthermore, the magnetic Reynolds number of the flow is considered to be low enough that the induced magnetic field is insignificant. Also, it is supposed that $y = A(x+b)^{((1-m)/2)}$, $U_w(x) = U_0(x+b)^m$, $\nu_w = 0$, $m \neq 1$. The physical model of the problem may be given in Figure 1.

The balance equations of motion for the Casson and Williamson model under the above assumptions are [26]

$$\frac{\partial u}{\partial x} + \frac{\partial v}{\partial y} = 0, \tag{2}$$

$$u\frac{\partial u}{\partial x} + v\frac{\partial u}{\partial y} = \nu\left(1+\frac{1}{\beta}\right)\frac{\partial^2 u}{\partial y^2} + \sqrt{2}\nu\Gamma\frac{\partial u}{\partial y}\frac{\partial^2 u}{\partial y^2} - \frac{\sigma B^2(x)}{\rho}u, \tag{3}$$

$$\begin{aligned} u\frac{\partial T}{\partial x} + v\frac{\partial T}{\partial y} = {} & \frac{1}{\rho c_p}\frac{\partial}{\partial y}\left(\kappa\frac{\partial T}{\partial y}\right) \\ & + \frac{\mu}{\rho c_p}\left(\left(1+\frac{1}{\beta}\right)\left(\frac{\partial u}{\partial y}\right)^2 + \frac{\Gamma}{\sqrt{2}}\left(\frac{\partial u}{\partial y}\right)^3\right) \\ & + \frac{Q}{\rho c_p}(T - T_\infty), \end{aligned} \tag{4}$$

$$u\frac{\partial C}{\partial x} + v\frac{\partial C}{\partial y} = D_m\frac{\partial^2 C}{\partial y^2}, \tag{5}$$

where $u$ and $v$ are the velocity components in the $x-$ and $y-$ directions, $\beta$ is the Casson fluid parameter, $T$ is the fluid temperature, $c_p$ is the specific heat, $\nu$ is the kinematic viscosity, $\kappa$ is the thermal conductivity of the fluid, which can be taken as $\kappa = \kappa_E(1+\varepsilon\theta)$ [7] which is a linear function of $\theta$ alone, $\mu_\infty$ is the dynamic viscosity away from the sheet, $\kappa_\infty$ is the thermal conductivity at the ambient, $\varepsilon$ is the thermal conductivity parameter, $\mu$ is the fluid viscosity, and $\rho$ is the density of the fluid. Also, $Q$, which appears in the last term of energy equation, is the coefficient of space-dependent internal heat generation. Likewise, we suppose that the fluid model possesses concentration $C$ with molecular diffusivity $D_m$.

We also express the boundary conditions in the following form [17]:

$$\begin{aligned} u &= U_w(x), \\ v &= 0, \\ -\kappa\frac{\partial T}{\partial y} &= h_w(T_w - T), \\ -D_m\frac{\partial C}{\partial y} &= h_s(C_w - C), \quad \text{at } y \end{aligned} \tag{6}$$

$$\begin{aligned} u &\longrightarrow 0, \\ T &\longrightarrow T_\infty, \\ C &\longrightarrow C_\infty, \quad \text{as } y \longrightarrow \infty, \end{aligned} \tag{7}$$

where $h_w$ and $h_s$ are the heat transfer coefficient and the concentration coefficient based on the resistance of the wall

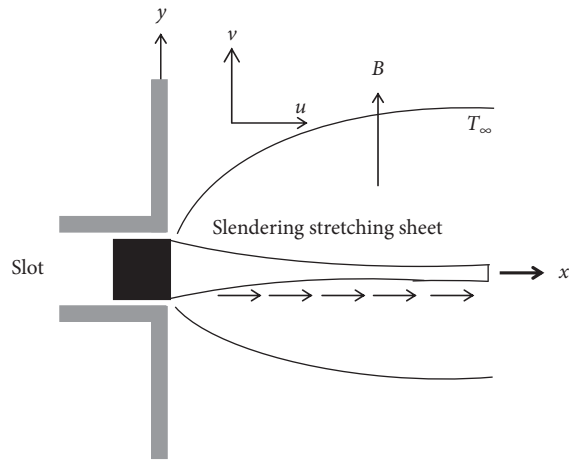


Figure 1: Physical model and coordinate system.

and ambient-side surface resistance, respectively, $C_w$ is the concentration at the surface, $T_\infty$ is the ambient temperature, and $T_w$ is temperature at the stretching sheet. It is interesting to note here that the heat convection is equal to the heat conduction at the stretching sheet, according to the third part of equation (6). Furthermore, the fourth part of the same equation states that mass convection at the sheet is equal to the rate of change in concentration in the $y$-direction.

It is convenient to introduce the following dimensionless variables [17]:

$$\eta = y\sqrt{U_0\left(\frac{m+1}{2}\right)\left(\frac{(x+b)^{m-1}}{\nu}\right)},$$
$$\psi(x,y) = \sqrt{\nu U_0\left(\frac{2}{m+1}\right)(x+b)^{m+1}}\, f(\eta), \tag{8}$$

$$\theta(\eta) = \left(\frac{T-T_\infty}{T_w-T_\infty}\right),$$
$$\phi(\eta) = \left(\frac{C-C_\infty}{C_w-C_\infty}\right), \tag{9}$$

where $\psi$ is a stream function which can be combine between $u, v$ as $u = (\partial\psi/\partial y)$ and $v = -(\partial\psi/\partial x)$. So, $u$ and $v$ satisfy the equation of the continuity and become as

$$u = U_0(x+b)^m f'(\eta),$$
$$v = -\sqrt{\frac{m+1}{2}\nu U_0(x+b)^{m-1}}\left[f'(\eta)\eta\left(\frac{m-1}{m+1}\right) + f(\eta)\right]. \tag{10}$$

In view of nondimensional quantities (equations (8)–(10)), equation (2) is identically satisfied, whereas equations (3)–(5) reduce to the following coupled, nonlinear, and dimensionless ordinary differential equations for momentum, energy, and concentration for the regime:

$$\left(1+\frac{1}{\beta}\right)f''' + f''f - \left(\frac{2m}{m+1}\right)f'^2 + \Lambda f''''Mf' = 0, \tag{11}$$

$$\frac{1}{\mathrm{Pr}}\left((1+\varepsilon\theta)\theta'' + \varepsilon\theta'^2\right) + f\theta' + Ec\left(\left(1+\frac{1}{\beta}\right) + \frac{\Lambda}{2}f''\right)f''^2 + \delta\theta \tag{12}$$

$$\frac{1}{\mathrm{Sc}}\phi'' + f\phi' = 0, \tag{13}$$

where $\Lambda = \Gamma\sqrt{(m+1)U_0^3((x+b)^{3m-1}/\nu)}$ is the local Williamson parameter, $M = (2\sigma B^2/\rho U_0(m+1))$ is the magnetic parameter, $\delta = (2Q(x+b)^{1-m}/(1+m)\rho c_p U_0)$ is the local heat generation parameter ( > rbin0) or the absorption parameter ( < 0), $\mathrm{Pr} = (\mu c_p/k)$ is the Prandtl number, $Ec = (U_w^2/c_p(T_w - T_\infty))$ is the Eckert number, and $\mathrm{Sc} = ((\nu/D_m))$ is the Schmidt number.

Likewise, the transformed dimensionless boundary conditions are

$$f(0) = 0,$$
$$f'(0) = 1,$$
$$\theta'(0) = -\gamma\left[\frac{1-\theta(0)}{1+\varepsilon\theta(0)}\right], \tag{14}$$
$$\phi'(0) = -\lambda[1-\phi(0)],$$

$$f'(\eta) \longrightarrow 0,$$
$$\theta(\eta) \longrightarrow 0, \tag{15}$$
$$\phi(\eta) \longrightarrow 0, \quad \text{as } \eta \longrightarrow \infty,$$

where $\gamma = (h_w\sqrt{2\nu}/\kappa\sqrt{(1+m)U_0(b+x)^{m-1}})$ is the thermal convective parameter and $\lambda = (h_s\sqrt{2\nu}/D_m\sqrt{(1+m)U_0(b+x)^{m-1}})$ is the mass convective parameter.

The engineering design quantities of physical interest include the local skin-friction coefficient $C_f$, the local Nusselt number $Nu_x$, and the local Sherwood number $Sh_x$, which are given by

$$C_f\sqrt{\mathrm{Re}_x} = -2\sqrt{\frac{m+1}{2}}\left(\left(1+\frac{1}{\beta}\right)f''(0) + \Lambda f''^2(0)\right),$$
$$\frac{Nu_x}{\sqrt{\mathrm{Re}_x}} = -\sqrt{\frac{m+1}{2}}\theta'(0), \tag{16}$$
$$\frac{Sh_x}{\sqrt{\mathrm{Re}_x}} = -\sqrt{\frac{m+1}{2}}\phi'(0),$$

where $\mathrm{Re}_x = (U_w X/\nu)$ is the local Reynolds number and $X = x + b$.

## 3. Basic Concepts on the Shifted Vieta–Lucas Polynomials

In this section of the study, we are presenting the basic definitions of the shifted Vieta–Lucas polynomials (VLPs), their notations, and properties that we will use in our study, and they are necessary to reach our goal [27].

We are researching a class of orthogonal polynomials, which lies at the heart of our research. Using the recurrence relations and analytical formulae of these polynomials, they can be generated to construct a new family of orthogonal polynomials that will be known as Vieta–Lucas polynomials.

The Vieta–Lucas polynomials, $\mathrm{VL}_m(z)$, of degree $m \in \mathbb{N}_0$ are defined by the following relation [27]:

$$\mathrm{VL}_m(z) = 2\cos(m\psi), \psi = \arccos\left(\frac{z}{2}\right), \quad \psi \in [0,\pi],\ |z| \le 2. \tag{17}$$

It is easy like other famous functions; one can prove that these Vieta–Lucas polynomials satisfy the following recurrence formula:

$$\begin{aligned} \mathrm{VL}_m(z) &= z\mathrm{VL}_{m-1}(z) - \mathrm{VL}_{m-2}(z), \\ m &= 2,3,\ldots, \quad VL_0(z) = 2,\ \mathrm{VL}_1(z) = z. \end{aligned} \tag{18}$$

Using the transformation, $z = 4x - 2$, we can generate from the family of Vieta–Lucas polynomials, a new class of orthogonal polynomials on the interval $[0,1]$, which is the orthogonal family of the shifted Vieta–Lucas polynomials, and it will be denoted by $\mathrm{VL}_m^*(x)$ and can be obtained as follows:

$$\mathrm{VL}_m^*(x) = \mathrm{VL}_m(4x-2). \tag{19}$$

The shifted Vieta–Lucas polynomials $\mathrm{VL}_m^*(x)$ satisfy the following recurrence relation:

$$\mathrm{VL}_{m+1}^*(x) = (4x-2)\mathrm{VL}_m^*(x) - \mathrm{VL}_{m-1}^*(x) \quad m = 1,2,\ldots, \tag{20}$$

where $\mathrm{VL}_0^*(x) = 2$ and $\mathrm{VL}_1^*(x) = 4x-2$. Also, we find $\mathrm{VL}_m^*(0) = 2(-1)^m$ and $\mathrm{VL}_m^*(1) = 2$, $m = 0,1,2,\ldots$.

The analytical formula for $\mathrm{VL}_m^*(x)$ is given by

$$\mathrm{VL}_m^*(x) = 2m\sum_{j=0}^{m}(-1)^j\frac{4^{m-j}\Gamma(2m-j)}{\Gamma(j+1)\Gamma(2m-2j+1)}x^{m-j}, \quad m = 2,3,\ldots. \tag{21}$$

The shifted Vieta–Lucas polynomials $\mathrm{VL}_m^*(x)$ are orthogonal polynomials on the interval $[0,1]$ with respect to the weight function $(1/\sqrt{x-x^2})$, so we have the following orthogonality property:

$$\left\langle \mathrm{VL}_m^*(x), \mathrm{VL}_n^*(x)\right\rangle = \int_0^1 \frac{\mathrm{VL}_m^*(x), \mathrm{VL}_n^*(x)}{\sqrt{x-x^2}}\mathrm{d}x = \begin{cases} 0, & n \neq m \neq 0, \\ 4\pi, & n = m = 0, \\ 2\pi, & n = m \neq 0. \end{cases} \tag{22}$$

Let $v(x)$ be a function in the space $L^2[0,1]$; then, using the shifted Vieta–Lucas polynomials $\mathrm{VL}_m^*(x)$, this function $v(x)$ can be written as follows:

$$v(x) = \sum_{j=0}^{\infty} c_j \mathrm{VL}_j^*(x), \tag{23}$$

where $c_j$ are the values that we should evaluate to express the function $v(x)$ in terms of the shifted Vieta–Lucas polynomials $\mathrm{VL}_m^*(x)$. Consider the first $m+1$ terms only of equation (23); then, we can write:

$$v_m(x) = \sum_{j=0}^{m} c_j \mathrm{VL}_j^*(x), \tag{24}$$

such that $c_j$, $j = 0,2,\ldots,m$, can be evaluated by using the following formula:

$$c_j = \frac{1}{\delta_j}\int_0^1 \frac{v(x)\mathrm{VL}_j^*(x)}{\sqrt{x-x^2}}\mathrm{d}x, \quad \delta_j = \begin{cases} 4\pi, & j = 0, \\ 2\pi, & j = 1,2,\ldots,m. \end{cases} \tag{25}$$

## 4. An Approximate of the $n$-Order Derivative and the Convergence Analysis

This section is devoted to presenting an approximate formula of the $n$-order derivative via shifted VLPs and studying the convergence analysis by computing the error estimate of the proposed approximation.

**Theorem 1.** *The n-order derivative for the function $v_m(x)$ which is defined in equation (24) can be computed by the following approximate formula [28]:*

$$v_m^{(n)}(x) = \sum_{j=n}^{m}\sum_{s=0}^{j-n} c_j \chi_{j,s,n} x^{j-s-n}, \tag{26}$$

*where*

$$\chi_{j,s,n} = (-1)^s \frac{4^{j-s}(2j)\Gamma(2j-s)\Gamma(j-s+1)}{\Gamma(s+1)\Gamma(2j-2s+1)\Gamma(j-s+1-v)}. \tag{27}$$

**Theorem 2.** *Assume that $v(x)$ belongs to the space of all Lebesgue-square-integrable on the interval $[0,1]$ with respect to the weight function $(1/\sqrt{x-x^2})$, and assume that the second derivative of $v(x)$ is a bounded function by the constant L (upper bound). Then, $v(x)$ can be written in terms of the shifted VLPs as a linear combination of $VL_m^*(x)$, and $v_m(x)$ contains $m+1$ terms only of this expression. Also, this series converges uniformly to the function $v(x)$ as $m \longrightarrow \infty$. Moreover, the coefficients given in equation (24) are bounded, i.e., [29]*

$$\left|c_j\right| \leq \frac{L}{4j\left(j^2-1\right)}, \quad j>2. \tag{28}$$

**Theorem 3.** *Assume that $v(x)$ satisfies the requirements of Theorem 2, and let the weight function in the orthogonality relation of the shifted VLPs on $[0,1]$ be the function $w(x) = (1/\sqrt{x-x^2})$; then, the norm of the error estimate ($L_w^2[0,1]$-norm) is given by [29]*

$$\left\|v(x)-v_m(x)\right\|_w < \frac{L}{12\sqrt{m^3}}. \tag{29}$$

**Theorem 4.** *Let $v(x)$ be an m-times continuously differentiable on $[0,1]$, and the most suitable approximation for $v(x)$ is $v_m(x)$ which is expressed in equation (24); then, we have the following absolute error bound [29]:*

$$\left\|v(x)-v_m(x)\right\| \leq \frac{\Delta\Omega^{m+1}}{(m+1)!}\sqrt{\pi}, \tag{30}$$

*where*

$$\begin{aligned} \Delta &= \max_{x\in[0,1]} v^{(m+1)}(x), \\ \Omega &= \max\{1-x_0, x_0\}. \end{aligned} \tag{31}$$

## 5. Procedure Solution Using SVLCOM

Here, we will implement the spectral collocation method based on a summation of Vieta–Lucas functions (VLFs) as a basis to convert the system of ODEs that describes the problem to a system of algebraic equations. This system is constructed as a constrained optimization problem and optimized to get the unknown coefficients of the series of the solution. This connection of the two well-known methods will be called "the shifted Vieta–Lucas collocation optimization method (SVLCOM)". The given problem (11)–(15) will be solved numerically by applying this technique through the following steps:

(1) We express and approximate the solution of problems (11)–(13) as a finite series of VLFs, namely,

$$\begin{aligned} f_N(\eta) &= \sum_{j=0}^{N} a_j \mathrm{VL}_j^*(\eta), \\ \theta_N(\eta) &= \sum_{j=0}^{N} b_j \mathrm{VL}_j^*(\eta), \\ \phi_N(\eta) &= \sum_{j=0}^{N} c_j \mathrm{VL}_j^*(\eta). \end{aligned} \tag{32}$$

(2) We substitute from (32) and the $n$-order derivatives defined by (26) in the proposed models (11)–(13) to obtain

$$\begin{aligned} &\left(1+\frac{1}{\beta}\right)\left(\sum_{j=3}^{N}\sum_{s=0}^{j-3} a_j\chi_{j,s,3}\eta^{j-s-3}\right)+\left(\sum_{j=2}^{N}\sum_{s=0}^{j-2} a_j\chi_{j,s,2}\eta^{j-s-2}\right)\left(\sum_{j=0}^{N} a_j\mathrm{VL}_j^*(\eta)\right) \\ &-\left(\frac{2m}{m+1}\right)\left(\sum_{j=1}^{N}\sum_{s=0}^{j-1} a_j\chi_{j,s,1}\eta^{j-s-1}\right)^2+\Lambda\left(\sum_{j=2}^{N}\sum_{s=0}^{j-2} a_j\chi_{j,s,2}\eta^{j-s-2}\right) \end{aligned} \tag{33}$$

$$\left(\sum_{j=3}^{N}\sum_{s=0}^{j-3} a_j\chi_{j,s,3}\eta^{j-s-3}\right)-M\left(\sum_{j=1}^{N}\sum_{s=0}^{j-1} a_j\chi_{j,s,1}\eta^{j-s-1}\right)=0, \tag{34}$$

$$\begin{aligned} &\frac{1}{\mathrm{Pr}}\left(\left(1+\varepsilon\left(\sum_{j=0}^{N} b_j\mathrm{VL}_j^*(\eta)\right)\right)\left(\sum_{j=2}^{N}\sum_{s=0}^{j-2} b_j\chi_{j,s,2}\eta^{j-s-2}\right)+\varepsilon\left(\sum_{j=1}^{N}\sum_{s=0}^{j-1} b_j\chi_{j,s,1}\eta^{j-s-1}\right)^2\right) \\ &+\left(\sum_{j=0}^{N} a_j\mathrm{VL}_j^*(\eta)\right)\left(\sum_{j=1}^{N}\sum_{s=0}^{j-1} b_j\chi_{j,s,1}\eta^{j-s-1}\right)+\mathrm{Ec} \end{aligned} \tag{35}$$

$$\left(\left(1+\frac{1}{\beta}\right)+\frac{\Lambda}{2}\left(\sum_{j=2}^{N}\sum_{s=0}^{j-2}a_j\chi_{j,s,2}\eta^{j-s-2}\right)\right)\left(\sum_{j=2}^{N}\sum_{s=0}^{j-2}a_j\chi_{j,s,2}\eta^{j-s-2}\right)^2+\delta\left(\sum_{j=0}^{N}b_j\mathrm{VL}_j^*(\eta)\right)=0, \tag{36}$$

$$\frac{1}{\mathrm{Sc}}\left(\sum_{j=2}^{N}\sum_{s=0}^{j-2}c_j\chi_{j,s,2}\eta^{j-s-2}\right)+\left(\sum_{j=0}^{N}a_j\mathrm{VL}_j^*(\eta)\right)\left(\sum_{j=1}^{N}\sum_{s=0}^{j-1}c_j\chi_{j,s,1}\eta^{j-s-1}\right)=0. \tag{37}$$

(3) The previous equations (33)–(37) will be collocated at $N-2$ of nodes at selected grid $\eta_k$, $k=0,1,2,\ldots,N-3$ as follows:

$$\left(1+\frac{1}{\beta}\right)\left(\sum_{j=3}^{N}\sum_{s=0}^{j-3}a_j\chi_{j,s,3}\eta_k^{j-s-3}\right)+\left(\sum_{j=2}^{N}\sum_{s=0}^{j-2}a_j\chi_{j,s,2}\eta_k^{j-s-2}\right)\left(\sum_{j=0}^{N}a_j\mathrm{VL}_j^*(\eta_k)\right)-\left(\frac{2m}{m+1}\right)\left(\sum_{j=1}^{N}\sum_{s=0}^{j-1}a_j\chi_{j,s,1}\eta_k^{j-s-1}\right)^2+\Lambda\left(\sum_{j=2}^{N}\sum_{s=0}^{j-2}a_j\chi_{j,s,2}\eta_k^{j-s-2}\right) \tag{38}$$

$$\left(\sum_{j=3}^{N}\sum_{s=0}^{j-3}a_j\chi_{j,s,3}\eta_k^{j-s-3}\right)-M\left(\sum_{j=1}^{N}\sum_{s=0}^{j-1}a_j\chi_{j,s,1}\eta_k^{j-s-1}\right)=0, \tag{39}$$

$$\frac{1}{\mathrm{Pr}}\left(\left(1+\varepsilon\left(\sum_{j=0}^{N}b_j\mathrm{VL}_j^*(\eta_k)\right)\right)\left(\sum_{j=2}^{N}\sum_{s=0}^{j-2}b_j\chi_{j,s,2}\eta_k^{j-s-2}\right)+\varepsilon\left(\sum_{j=1}^{N}\sum_{s=0}^{j-1}b_j\chi_{j,s,1}\eta_k^{j-s-1}\right)^2\right)+\left(\sum_{j=0}^{N}a_j\mathrm{VL}_j^*(\eta_k)\right)\left(\sum_{j=1}^{N}\sum_{s=0}^{j-1}b_j\chi_{j,s,1}\eta_k^{j-s-1}\right)+\mathrm{Ec}, \tag{40}$$

$$\left(\left(1+\frac{1}{\beta}\right)+\frac{\Lambda}{2}\left(\sum_{j=2}^{N}\sum_{s=0}^{j-2}a_j\chi_{j,s,2}\eta_k^{j-s-2}\right)\right)\left(\sum_{j=2}^{N}\sum_{s=0}^{j-2}a_j\chi_{j,s,2}\eta_k^{j-s-2}\right)^2+\delta\left(\sum_{j=0}^{N}b_j\mathrm{VL}_j^*(\eta_k)\right)=0, \tag{41}$$

$$\frac{1}{\mathrm{Sc}}\left(\sum_{j=2}^{N}\sum_{s=0}^{j-2}c_j\chi_{j,s,2}\eta_k^{j-s-2}\right)+\left(\sum_{j=0}^{N}a_j\mathrm{VL}_j^*(\eta_k)\right)\left(\sum_{j=1}^{N}\sum_{s=0}^{j-1}c_j\chi_{j,s,1}\eta_k^{j-s-1}\right)=0. \tag{42}$$

The boundary conditions (14)-(15) can be approximated at the finite interval $(0,\eta_\infty)$ as follows:

$$\begin{aligned}
&\sum_{j=0}^{N}2(-1)^j a_j=0,\\
&\sum_{j=0}^{N}a_j\mathrm{VL}_j^{*'}(0)=1,\\
&\sum_{j=0}^{N}b_j\mathrm{VL}_j^{*'}(0)=-\gamma\left[\frac{1-\sum_{j=0}^{N}2(-1)^j b_j}{1+\varepsilon\sum_{j=0}^{N}2(-1)^j b_j}\right],\\
&\sum_{j=0}^{N}c_j\mathrm{VL}_j^{*'}(0)=-\lambda\left[1-\sum_{j=0}^{N}2(-1)^j c_j\right],\\
&\sum_{j=0}^{N}a_j\mathrm{VL}_j^{*'}(\eta_\infty)=0,\\
&\sum_{j=0}^{N}2b_j=0,\\
&\sum_{j=0}^{N}2c_j=0.
\end{aligned} \tag{43}$$

(44)

(45)

(4) We express the problem defined by (38)–(45) as a constrained optimization problem with the following cost functions (CFs):

$$\mathrm{CF1} = \sum_{k=0}^{N} \left| \left(1 + \frac{1}{\beta}\right)\left(\sum_{j=3}^{N}\sum_{s=0}^{j-3} a_j \chi_{j,s,3} \eta_k^{j-s-3}\right) + \left(\sum_{j=2}^{N}\sum_{s=0}^{j-2} a_j \chi_{j,s,2} \eta_k^{j-s-2}\right)\left(\sum_{j=0}^{N} a_j \mathrm{VL}_j^*(\eta_k)\right) - \left(\frac{2m}{m+1}\right)\left(\sum_{j=1}^{N}\sum_{s=0}^{j-1} a_j \chi_{j,s,1} \eta_k^{j-s-1}\right)^2 + \Lambda\left(\sum_{j=2}^{N}\sum_{s=0}^{j-2} a_j \chi_{j,s,2} \eta_k^{j-s-2}\right) \right. \tag{46}$$

$$\left. \left(\sum_{j=3}^{N}\sum_{s=0}^{j-3} a_j \chi_{j,s,3} \eta_k^{j-s-3}\right) - M\left(\sum_{j=1}^{N}\sum_{s=0}^{j-1} a_j \chi_{j,s,1} \eta_k^{j-s-1}\right) \right|, \tag{47}$$

$$\mathrm{CF2} = \sum_{k=0}^{N} \left| \left(1 + \varepsilon\left(\sum_{j=0}^{N} b_j \mathrm{VL}_j^*(\eta_k)\right)\right)\left(\sum_{j=2}^{N}\sum_{s=0}^{j-2} b_j \chi_{j,s,2} \eta_k^{j-s-2}\right) + \varepsilon\left(\sum_{j=1}^{N}\sum_{s=0}^{j-1} b_j \chi_{j,s,1} \eta_k^{j-s-1}\right)^2 + \mathrm{Pr}\left(\sum_{j=0}^{N} a_j \mathrm{VL}_j^*(\eta_k)\right)\left(\sum_{j=1}^{N}\sum_{s=0}^{j-1} b_j \chi_{j,s,1} \eta_k^{j-s-1}\right) + \mathrm{EcPr} \right. \tag{48}$$

$$\left. \left(\left(1 + \frac{1}{\beta}\right) + \frac{\Lambda}{2}\left(\sum_{j=2}^{N}\sum_{s=0}^{j-2} a_j \chi_{j,s,2} \eta_k^{j-s-2}\right)\right)\left(\sum_{j=2}^{N}\sum_{s=0}^{j-2} a_j \chi_{j,s,2} \eta_k^{j-s-2}\right)^2 + \delta\mathrm{Pr}\left(\sum_{j=0}^{N} b_j \mathrm{VL}_j^*(\eta_k)\right) \right|, \tag{49}$$

$$\mathrm{CF3} = \sum_{k=0}^{N} \left| \frac{1}{\mathrm{Sc}}\left(\sum_{j=2}^{N}\sum_{s=0}^{j-2} c_j \chi_{j,s,2} \eta_k^{j-s-2}\right) + \left(\sum_{j=0}^{N} a_j \mathrm{VL}_j^*(\eta_k)\right)\left(\sum_{j=1}^{N}\sum_{s=0}^{j-1} c_j \chi_{j,s,1} \eta_k^{j-s-1}\right) \right|, \tag{50}$$

and the constraints (Cons.) are

$$\begin{aligned} \mathrm{Cons.} = &\left|\sum_{j=0}^{N} 2(-1)^j a_j\right| + \left|\sum_{j=0}^{N} a_j \mathrm{VL}_j^{*'}(0) - 1\right| + \left|\sum_{j=0}^{N} b_j \mathrm{VL}_j^{*'}(0) + \gamma\left[\frac{1 - \sum_{j=0}^{N} 2(-1)^j b_j}{1 + \varepsilon\sum_{j=0}^{N} 2(-1)^j b_j}\right]\right| \\ &+ \left|\sum_{j=0}^{N} c_j \mathrm{VL}_j^{*'}(0) + \lambda\left[1 - \sum_{j=0}^{N} 2(-1)^j c_j\right]\right| + \left|\sum_{j=0}^{N} a_j \mathrm{VL}_j^{*'}(\eta_\infty)\right| + \left|\sum_{j=0}^{N} 2b_j\right| + \left|\sum_{j=0}^{N} 2c_j\right|. \end{aligned} \tag{51}$$

(5) We use the Penalty Leap Frog procedure [30] for solving the constrained optimization problem (46)–(51) for the unknowns $a_j, b_j, c_j,\ j = 0, 1, 2, \ldots, N$. Then, we can construct the approximate solution by using formula (32).

## 6. Validation of the SVLCOM

The goal of this section is to demonstrate the accuracy and reliability of the numerical values acquired through the SVLCOM. Clearly, the comparison is carried out for the values of the skin-friction coefficient with different values of $\Lambda$. This verification is suggested in Table 1, which shows that the current results are in excellent accord with previously published benchmark data [17].

## 7. Results and Discussion

In order to study the effects of the different parameters on the MHD Casson and Williamson fluid flow, numerical calculations are carried out for different values of the parameters $M$, $\beta$, $\Lambda$, $\varepsilon$, Ec, $\delta$, $\gamma$, and $\lambda$. The magnetic parameter, $M$, describes the effects of the magnetic field in the fluid flow and heat transfer. $\beta$ describes the effects of the Casson parameter, $\Lambda$ is the local Williamson parameter, $\varepsilon$ is a parameter which describes the fluid thermal conductivity, Ec is

Table 1: Comparison of $(-1/2)\sqrt{(2/m+1)}C_f\sqrt{\mathrm{Re}_x}$ with the results of Abbas and Megahed [17] when $M = 0.5$, $\beta = 1.5$, and $m = 0.5$.

| $\Lambda$ | Abbas and Megahed [17] | Present work |
|---|---|---|
| 0.0 | 1.46382 | 1.4638174890 |
| 0.5 | 0.83281 | 0.8327981903 |
| 1.0 | 0.41518 | 0.4151684879 |

called Eckert number, $\delta$ describes the effects of the heat generation parameter, $\gamma$ is the thermal convective parameter, and $\lambda$ is the mass convective parameter. In Figure 2, the velocity distribution $f'(\eta)$ is plotted against $\eta$ for different values of $M$. It is observed that an increase in $M$ leads to a decrease in both velocity distribution and boundary layer thickness.

The graphs of the temperature distribution have been plotted against $\eta$ for the same parameter $M$ in Figure 3. It is found from Figure 3 that, as the magnetic number increases, the thermal boundary layer thickness growth is enhanced. The effect of the magnetic number is considered to increase the temperature field as well as the sheet temperature $\theta(0)$ considerably. The effect of magnetic number on these fluid flow and heat transfer characteristics are more significant. Physically, an increase in magnetic field strength accelerates the Lorentz force, which causes fluid particles to encounter greater resistance, lowering fluid velocity. Because of the presence of this force, friction between the fluid layers increases, resulting in an increase in fluid temperature.

Another remarkable effect of magnetic parameter $M$ is observed in thickening the boundary layer and in enhancing the concentration along the sheet $\phi(0)$ as observed from Figure 4. On the contrary, the concentration distribution mechanism of the non-Newtonian fluid increases with magnetic parameter due to excess of concentration generated by mass convective phenomenon.

The velocity profiles $f'(\eta)$ for some representative values of the Casson parameter $\beta$ are given in Figure 5. An important feature that is observed is that the velocity profiles $f'(\eta)$ decreases with increasing the Casson parameter $\beta$ which results in slimming the boundary layer thickness.

Figure 6 presents the effect of the Casson parameter $\beta$ on the temperature profiles $\theta(\eta)$ when other parameters are fixed. Clearly, the thermal boundary layer thicknesses increase significantly with the increase in Casson parameter $\beta$ results in an enhancement in the temperature distribution through the thermal boundary layer. On the contrary, cooling process for the stretching sheet can be achieved with Casson fluids having small $\beta$. Physically, increasing the Casson parameter brings the fluid properties closer to the Williamson type, which means more energy is created, which improves sheet temperature and thermal boundary thickness.

The numerical values of the Casson parameter $\beta$ are entered in Figure 7. In this figure, the concentration profiles $\phi(\eta)$ are presented against the similarity variable $\eta$. We further observe that, owing to increase in the Casson parameter $\beta$, there is an increase in both the concentration of the fluid along the sheet and the boundary layer thickness.

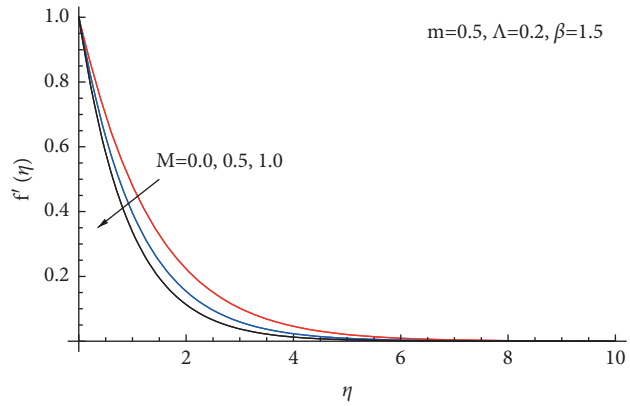


Figure 2: Influence of $M$ on $f'(\eta)$.

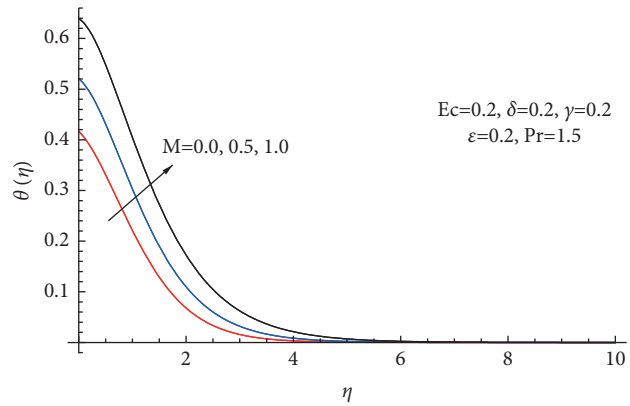


Figure 3: Influence of $M$ on $\theta(\eta)$.

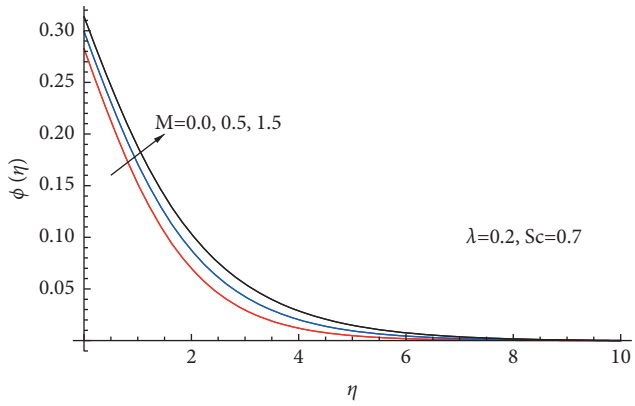


Figure 4: Influence of $M$ on $\phi(\eta)$.

In Figure 8, the velocity distribution $f'(\eta)$ is drawn against $\eta$ for various values of $\Lambda$. It is noted that an increase in $\Lambda$ leads to a slight decrease in velocity distribution through the boundary layer region. Physically, $\Lambda$ is proportional to the Williamson coefficient $\Gamma$, which is based on time; thus, a high Williamson coefficient of any substance makes it more viscous, which might result in a reduction in motion.

For different values of the local Williamson parameter $\Lambda$, the profiles of the temperature $\theta(\eta)$ against $\eta$ are shown in

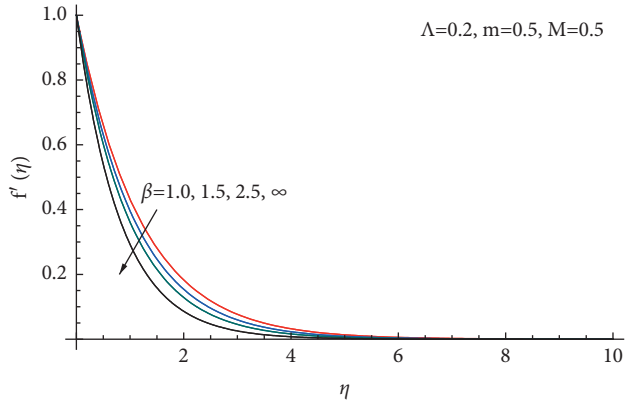


Figure 5: Influence of $\beta$ on $f'(\eta)$.

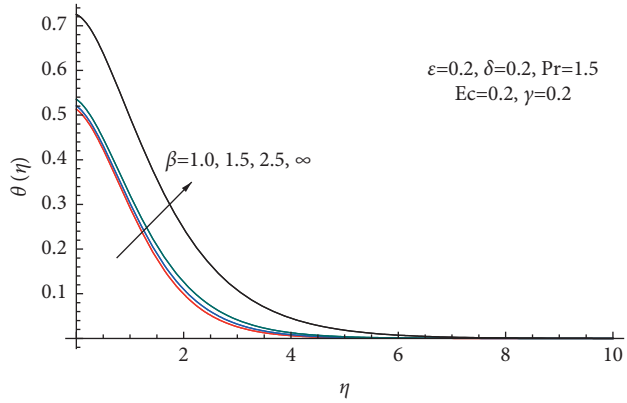


Figure 6: Influence of $\beta$ on $\theta(\eta)$.

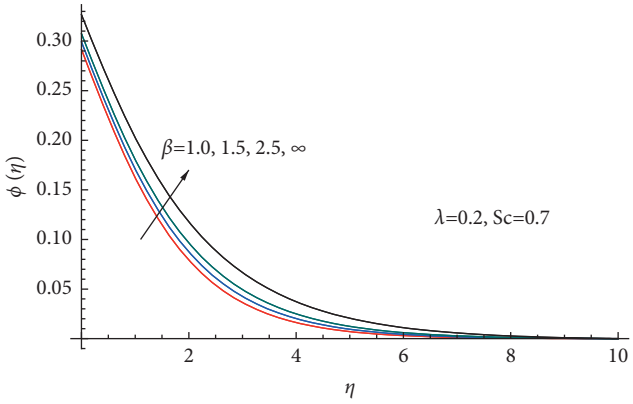


Figure 7: Influence of $\beta$ on $\phi(\eta)$.

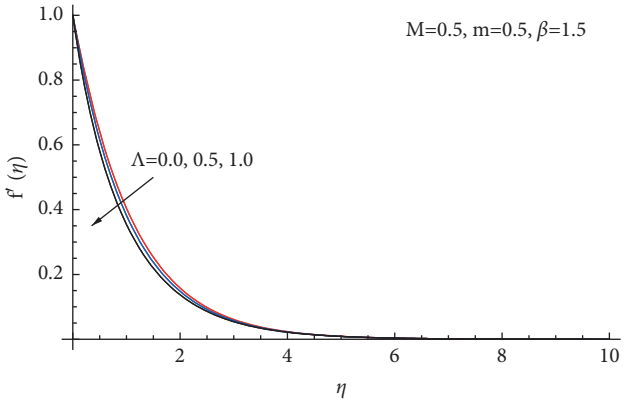


Figure 8: Influence of $\Lambda$ on $f'(\eta)$.

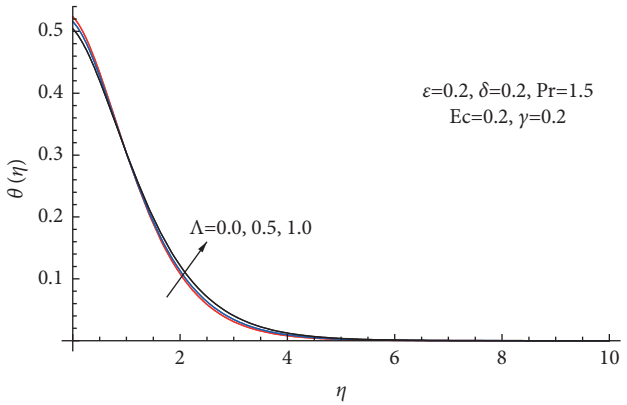


Figure 9: Influence of $\Lambda$ on $\theta(\eta)$.

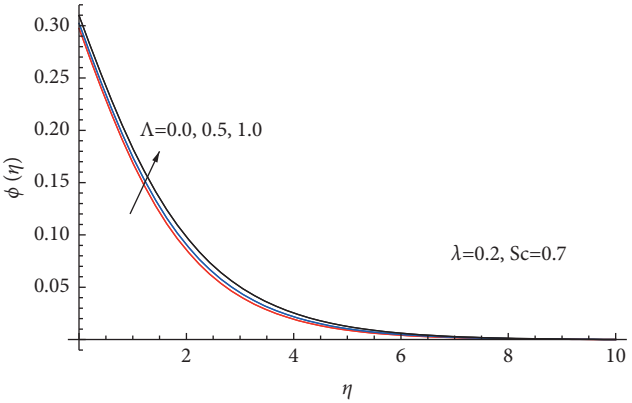


Figure 10: Influence of $\Lambda$ on $\phi(\eta)$.

Figure 9. It should be noted here that, away from the sheet, an increase in the value of the local Williamson parameter $\Lambda$ leads to an increase in the temperature distribution, but the reverse behavior is noted beside the sheet.

Figure 10 shows the interesting results of the local Williamson parameter $\Lambda$ on the concentration profiles $\phi(\eta)$ which have a slight effect on both the concentration distribution and on the rate of mass transfer.

Figure 11 shows the distribution of the temperature profiles $\theta(\eta)$ relative to the thermal conductivity parameter $\varepsilon$. Clearly, this parameter has a pronounced effect on the heat transfer mechanism especially away from the sheet, but only a slight reversed effect is observed for the sheet temperature beside the sheet. When the fluid thermal conductivity goes up due to a rise in temperature, the fluid temperature within the thermal layer effectively rises.

To observe the heat behavior $\theta(\eta)$ for different values of Eckert number $Ec$, Figure 12 against $\eta$ is presented. From this figure, we observe that the sheet temperature $\theta(\eta)$, the thermal thickness, and the temperature distribution increase

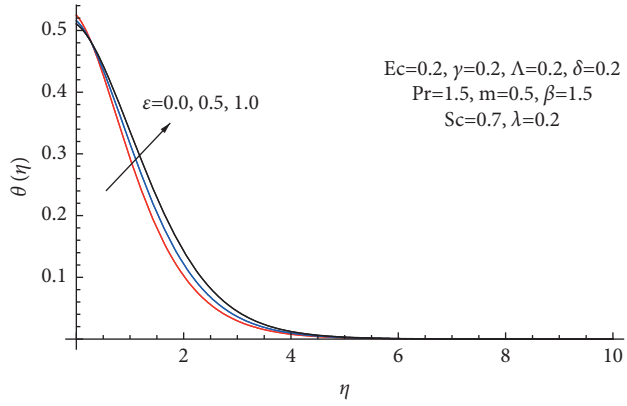


Figure 11: Influence of $\varepsilon$ on $\theta(\eta)$.

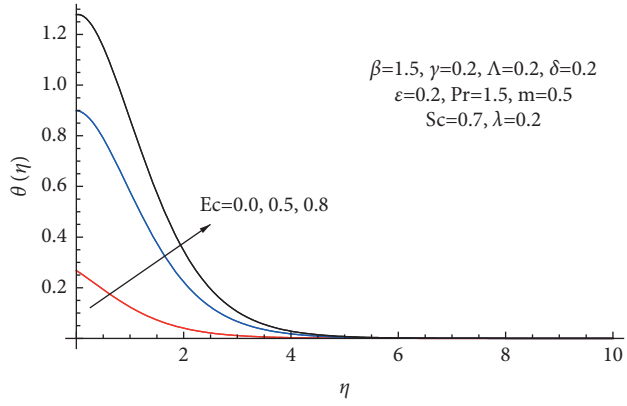


Figure 12: Influence of Ec on $\theta(\eta)$.

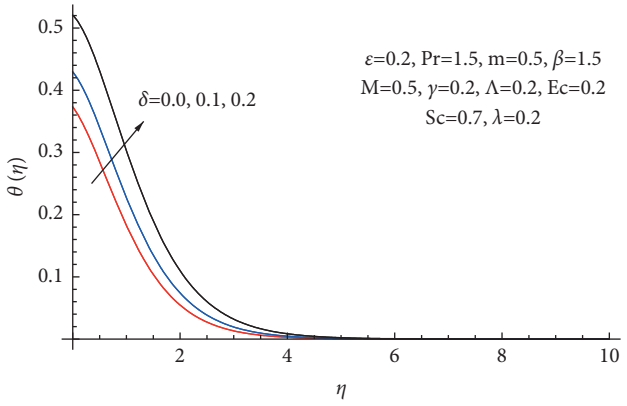


Figure 13: Influence of $\delta$ on $\theta(\eta)$.

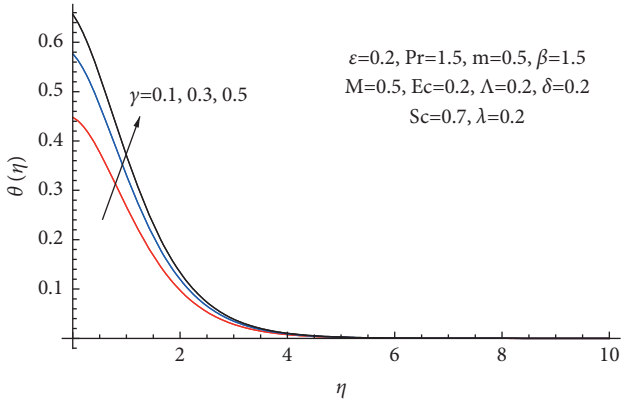


Figure 14: Influence of $\gamma$ on $\theta(\eta)$.

with the increase in Ec. The same behavior is observed in Figure 13 for various values of $\delta$, where an increase in the heat generation parameter $\delta$, leads to a slowly increase in the temperature distribution, the sheet temperature $\theta(\eta)$, and the thermal thickness. Physically, increasing the size of the Eckert number or the internal heat generation parameter produces a large amount of heat, which raises the fluid temperature.

The numerical values of the dimensionless temperature distributions are shown graphically in Figure 14 against $\eta$ at $\gamma = 0.1,\ 0.3,\ 0.5$. From this figure, we observed that the fluid temperature profiles increase with the increase in the thermal convective parameter $\gamma$. It can also be observed that the warming process for the sheet more pronounced for great values of the thermal convective parameter $\gamma$. Physically, the thermal convective phenomenon can be read as an average heat energy, and in this way, a rise in the thermal convective parameter results in a boost in heat energy, so both the sheet temperature and the temperature throughout the thermal layer raise.

The effects of varying the mass convective parameter, $\lambda = 0.1, 0.3, 0.5$, on the dimensionless concentration $\phi(\eta)$ against $\eta$, are shown in Figure 15. This figure shows that when the mass convective parameter $\lambda$ increases, the concentration profile increases. Likewise, we can see that, for smaller $\lambda$, the concentration of the fluid beside the sheet

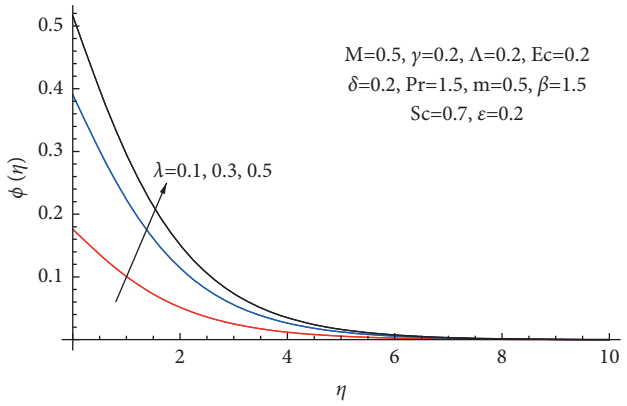


Figure 15: Influence of $\lambda$ on $\phi(\eta)$.

becomes less concentrated. We further observe that the boundary layer thickness increases with the increasing values of $\lambda$.

The numerical results are shown in Table 2 to give the values of the local skin-friction coefficient, the heat transfer rate, and the mass transfer rate relative to the governing parameters. It is seen from this table that the local skin-friction coefficient increases with the increase of the magnetic number and decreases with the increase of the local Williamson parameter and the Casson parameter. Also, both

Table 2: Variation of $(1/2)\sqrt{(2/m+1)}C_f\sqrt{\mathrm{Re}_x}$, $-\theta'(0)$ and $-\phi'(0)$ for various values of $M$, $\beta$, $\Lambda$, $\varepsilon$, Ec, $\delta$, $\gamma$, and $\lambda$ with $m = 0.5$, Pr = 1.5, and Sc = 0.7.

| $M$ | $\beta$ | $\Lambda$ | $\varepsilon$ | Ec | $\delta$ | $\gamma$ | $\lambda$ | $(-1/2)\sqrt{(2/m+1)}C_f\sqrt{\mathrm{Re}_x}$ | $-\theta'(0)$ | $-\phi'(0)$ |
|---|---|---|---|---|---|---|---|---|---|---|
| 0.0 | 1.5 | 0.2 | 0.2 | 0.2 | 0.2 | 0.2 | 0.2 | 1.0129951 | 0.107672 | 0.143506 |
| 0.5 | 1.5 | 0.2 | 0.2 | 0.2 | 0.2 | 0.2 | 0.2 | 1.2415185 | 0.086845 | 0.140181 |
| 1.5 | 1.5 | 0.2 | 0.2 | 0.2 | 0.2 | 0.2 | 0.2 | 1.4121084 | 0.063989 | 0.137295 |
| 0.5 | 1.0 | 0.2 | 0.2 | 0.2 | 0.2 | 0.2 | 0.2 | 1.3762085 | 0.088327 | 0.141701 |
| 0.5 | 1.5 | 0.2 | 0.2 | 0.2 | 0.2 | 0.2 | 0.2 | 1.2415185 | 0.086845 | 0.140180 |
| 0.5 | 2.5 | 0.2 | 0.2 | 0.2 | 0.2 | 0.2 | 0.2 | 1.1248884 | 0.083934 | 0.138529 |
| 0.5 | 1.5 | 0.0 | 0.2 | 0.2 | 0.2 | 0.2 | 0.2 | 1.4638175 | 0.086272 | 0.140533 |
| 0.5 | 1.5 | 0.5 | 0.2 | 0.2 | 0.2 | 0.2 | 0.2 | 0.8327982 | 0.087814 | 0.139562 |
| 0.5 | 1.5 | 1.0 | 0.2 | 0.2 | 0.2 | 0.2 | 0.2 | 0.4151685 | 0.090119 | 0.138088 |
| 0.5 | 1.5 | 0.2 | 0.0 | 0.2 | 0.2 | 0.2 | 0.2 | 1.2415185 | 0.095060 | 0.140181 |
| 0.5 | 1.5 | 0.2 | 0.5 | 0.2 | 0.2 | 0.2 | 0.2 | 1.2415185 | 0.076994 | 0.140181 |
| 0.5 | 1.5 | 0.2 | 1.0 | 0.2 | 0.2 | 0.2 | 0.2 | 1.2415185 | 0.064791 | 0.140181 |
| 0.5 | 1.5 | 0.2 | 0.2 | 0.0 | 0.2 | 0.2 | 0.2 | 1.2415185 | 0.139055 | 0.140181 |
| 0.5 | 1.5 | 0.2 | 0.2 | 0.5 | 0.2 | 0.2 | 0.2 | 1.2415185 | 0.017036 | 0.140181 |
| 0.5 | 1.5 | 0.2 | 0.2 | 0.8 | 0.2 | 0.2 | 0.2 | 1.2415185 | 0.004296 | 0.140181 |
| 0.5 | 1.5 | 0.2 | 0.2 | 0.2 | 0.0 | 0.2 | 0.2 | 1.2415185 | 0.116676 | 0.140181 |
| 0.5 | 1.5 | 0.2 | 0.2 | 0.2 | 0.1 | 0.2 | 0.2 | 1.2415185 | 0.105116 | 0.140181 |
| 0.5 | 1.5 | 0.2 | 0.2 | 0.2 | 0.2 | 0.2 | 0.2 | 1.2415185 | 0.086845 | 0.140181 |
| 0.5 | 1.5 | 0.2 | 0.2 | 0.2 | 0.2 | 0.1 | 0.2 | 1.2415185 | 0.050708 | 0.140181 |
| 0.5 | 1.5 | 0.2 | 0.2 | 0.2 | 0.2 | 0.3 | 0.2 | 1.2415185 | 0.113941 | 0.140181 |
| 0.5 | 1.5 | 0.2 | 0.2 | 0.2 | 0.2 | 0.5 | 0.2 | 1.2415185 | 0.151911 | 0.140181 |
| 0.5 | 1.5 | 0.2 | 0.2 | 0.2 | 0.2 | 0.2 | 0.1 | 1.2415185 | 0.086845 | 0.082415 |
| 0.5 | 1.5 | 0.2 | 0.2 | 0.2 | 0.2 | 0.2 | 0.3 | 1.2415185 | 0.086845 | 0.182915 |
| 0.5 | 1.5 | 0.2 | 0.2 | 0.2 | 0.2 | 0.2 | 0.5 | 1.2415185 | 0.086845 | 0.241914 |

the heat transfer rate and the mass transfer rate appear to become greater as the Casson parameter and the magnetic number increases. Furthermore, for increasing the thermal conductivity parameter, the Eckert number, and the heat generation parameter, the effects towards the heat transfer rate become smaller. Additionally, the greater the thermal convective parameter and the mass convective parameter, the more strongly the the heat transfer rate and the mass transfer rate.

## 8. Conclusions

The following conclusions can be drawn concerning approximate techniques applied to the Casson and Williamson model for the fluid flow and heat and mass transfer over a stretching sheet with convective wall temperature and convective wall mass boundary condition in the presence of a magnetic field and heat generation for the range of parameters studied. The main findings of our study on the Casson and Williamson model are as follows:

(1) The dimensionless velocity decreases with increasing the local Williamson parameter, magnetic parameter, and Casson parameter

(2) The magnetic number and the Casson parameter enhance both the temperature of the sheet and the temperature profiles

(3) The thermal convective parameter, the Eckert number, and the heat generation parameter have prominent effect on the temperature field

(4) Eminent influence on the concentration field is observed due to the presence of the magnetic parameter and the mass convective parameter

(5) In the future, we decide to develop on this research by looking at the effects of heat and mass fluxes on this sort of fluid, as well as the use of a porous medium to control the cooling process, which is critical in many industrial applications

## Nomenclature

$b$: Constant (m)
$B$: Strength of a uniform magnetic field (T)
$C$: Fluid concentration ($\mathrm{mol{\cdot}L^{-1}}$)
$c_p$: Specific heat at a constant pressure ($\mathrm{Jkg^{-1}K^{-1}}$)
$C_f$: Skin-friction coefficient
$C_w$: Fluid concentration at the sheet ($\mathrm{mol{\cdot}L^{-1}}$)
$C_\infty$: Fluid concentration away from the sheet ($\mathrm{mol{\cdot}L^{-1}}$)
$D_m$: Molecular diffusivity ($\mathrm{m^2s^{-1}}$)
Ec: Eckret number
$f$: Dimensionless stream function
$h_s$: Mass transfer coefficient ($\mathrm{ms^{-1}}$)
$h_w$: Heat transfer coefficient ($\mathrm{Wm^{-2}K^{-1}}$)
$M$: Magnetic parameter
$Nu_x$: Local Nusselt number
Pr: Prandtl number
Q: Coefficient of heat generation or absorption ($\mathrm{JK^{-1}m^{-3}s^{-1}}$)
$\mathrm{Re_x}$: Local Reynolds number
Sc: Schmidt number

$T$: Nanofluid temperature (K)
$T_w$: Surface temperature (K)
$T_\infty$: Ambient temperature (K)
$u$: Velocity component in the $x$-direction ($ms^{-1}$)
$U_w$: Sheet velocity ($ms^{-1}$)
$v$: Velocity component in the $y$-direction ($ms^{-1}$)
$x$, $y$: Cartesian coordinates (m)

*Greek symbols*
$\upsilon$: Kinematic viscosity ($m^{-2}s^{-1}$)
$\kappa$: Thermal conductivity ($Wm^{-1}K^{-1}$)
$\mu$: Coefficient of viscosity ($kgm^{-1}s^{-1}$)
$\rho$: Density of the fluid ($kgm^{-3}$)
$\phi$: Dimensionless concentration
$\theta$: Dimensionless temperature
$\gamma$: Thermal convective parameter
$\sigma$: Electrical conductivity ($Sm^{-1}$)
$\beta$: Casson parameter
$\lambda$: Mass convective parameter
$\Gamma$: Williamson coefficient (s)
$\Lambda$: Williamson parameter
$\delta$: Heat generation parameter
$\eta$: Similarity variable

*Superscripts*
$'$: Differentiation with respect to $\eta$
$\infty$: Free stream condition
$w$: Wall condition.

## Data Availability

No data were used to support this study.

## Conflicts of Interest

The authors declare that they have no conflicts of interest.

## Authors' Contributions

All authors contributed equally and significantly in writing this article. All authors read and approved the final manuscript.

## Acknowledgments

The authors extend their appreciation to the Deanship of Scientific Research at Imam Mohammad Ibn Saud Islamic University for funding this work through research group no. RG-21-09-06.

## References

[1] N. Casson, "A flow equation for pigment oil suspensions of printing ink type," *Rheology of Dispersed System*, Pergamon Press, Oxford, UK, 1959.
[2] M. Mustafa, T. Hayat, I. Pop, and A. Aziz, "Unsteady boundary layer flow of a Casson fluid due to an impulsively started moving flat plate," *Heat Transfer-Asian Research*, vol. 40, no. 6, pp. 563–576, 2011.
[3] R. K. Dash, K. N. Mehta, and G. Jayaraman, "Casson fluid flow in a pipe filled with a homogeneous porous medium," *International Journal of Engineering Science*, vol. 34, no. 10, pp. 1145–1156, 1996.
[4] S. Mukhopadhyay, P. R. De, K. Bhattacharyya, and G. C. Layek, "Casson fluid flow over an unsteady stretching surface," *Ain Shams Engineering Journal*, vol. 4, no. 4, pp. 933–938, 2013.
[5] A. M. Megahed, "Effect of slip velocity on Casson thin film flow and heat transfer due to unsteady stretching sheet in presence of variable heat flux and viscous dissipation," *Applied Mathematics and Mechanics*, vol. 36, no. 10, pp. 1273–1284, 2015.
[6] A. M. Megahed, "Heat flux and variable thermal conductivity effects on Casson flow and heat transfer due to an exponentially stretching sheet with viscous dissipation and heat generation," *International Journal of Chemical Reactor Engineering*, vol. 14, no. 1, pp. 167–174, 2016.
[7] M. A. A. Mahmoud and A. M. Megahed, "MHD flow and heat transfer characteristics in a Casson liquid film towards an unsteady stretching sheet with temperature-dependent thermal conductivity," *Brazilian Journal of Physics*, vol. 47, no. 5, pp. 512–523, 2017.
[8] R. V. Williamson, "The flow of pseudoplastic materials," *Industrial & Engineering Chemistry*, vol. 21, no. 11, pp. 1108–1111, 1929.
[9] S. Nadeem, S. T. Hussain, and C. Lee, "Flow of a Williamson fluid over a stretching sheet," *Brazilian Journal of Chemical Engineering*, vol. 30, no. 3, pp. 619–625, 2013.
[10] N. A. Khan and H. Khan, "A Boundary layer flows of non-Newtonian Williams on fluid," *Nonlinear Engineering*, vol. 3, no. 2, pp. 107–115, 2014.
[11] M. Y. Malik and T. Salahuddin, "Numerical solution of MHD stagnation point flow of Williamson fluid model over a stretching cylinder," *International Journal of Nonlinear Sciences and Numerical Simulation*, vol. 16, no. 3-4, pp. 161–164, 2015.
[12] M. Y. Malik, M. Bibi, F. Khan, and T. Salahuddin, "Numerical solution of Williamson fluid flow past a stretching cylinder and heat transfer with variable thermal conductivity and heat generation/absorption," *AIP Advances*, vol. 6, no. 3, 2016.
[13] C. Vittal, M. C. K. Reddy, and T. Vijayalaxmi, "MHD stagnation point flow and heat transfer of Williamson fluid over exponential stretching sheet embedded in a thermally stratified medium," *Global Journal of Pure and Applied Mathematics*, vol. 13, pp. 2033–2056, 2017.
[14] A. M. Megahed, "Williamson fluid flow due to a nonlinearly stretching sheet with viscous dissipation and thermal radiation," *Journal of the Egyptian Mathematical Society*, vol. 27, no. 1, pp. 12–16, 2019.
[15] A. M. Megahed, "Steady flow of MHD Williamson fluid due to a continuously moving surface with viscous dissipation and slip velocity," *International Journal of Modern Physics C*, vol. 31, no. 1, 2020.
[16] P. P. Humane, V. S. Patil, and A. B. Patil, "Chemical reaction and thermal radiation effects on magnetohydrodynamics flow of casson-Williamson nanofluid over a porous stretching surface," *Proceedings of the Institution of Mechanical Engineers, Part E: Journal of Process Mechanical Engineering*, vol. 235, no. 6, 2021.
[17] W. Abbas and A. M. Megahed, "Numerical solution for chemical reaction and viscous dissipation phenomena on non-Newtonian MHD fluid flow and heat mass transfer due to a non uniform stretching sheet with thermal radiation," *International Journal of Modern Physics C*, vol. 32, no. 9, Article ID 2150124, 2021.

[18] M. M. Khader and M. M. Babatin, "Numerical treatment for solving fractional SIRC model and influenza A," *Computational and Applied Mathematics*, vol. 33, no. 3, pp. 543–556, 2014.

[19] M. M. Khader and K. M. Saad, "On the numerical evaluation for studying the fractional KdV, KdV-Burger's and Burgers' equations," *The European Physical Journal Plus*, vol. 133, no. 8, pp. 1–13, 2018.

[20] M. M. Khader and K. M. Saad, "A numerical study by using the Chebyshev collocation method for a problem of biological invasion: fractional fisher equation," *International Journal of Biomathematics*, vol. 11, no. 8, pp. 1–15, 2018.

[21] K. M. Saad, M. M. Khader, J. F. Gómez-Aguilar, and D. Baleanu, "Numerical solutions of the fractional fisher's type equations with Atangana-Baleanu fractional derivative by using spectral collocation methods," *Chaos: An Interdisciplinary Journal of Nonlinear Science*, vol. 29, no. 2, 2019.

[22] M. M. Khader and K. M. Saad, "A numerical approach for solving the fractional fisher equation using Chebyshev spectral collocation method," *Chaos, Solitons & Fractals*, vol. 110, pp. 169–177, 2018.

[23] M. M. Khader, "On the numerical solutions for the fractional diffusion equation," *Communications in Nonlinear Science and Numerical Simulation*, vol. 16, no. 6, pp. 2535–2542, 2011.

[24] M. M. Khader and M. Adel, "Numerical and theoretical treatment based on the compact finite difference and spectral collocation algorithms of the space fractional-order fisher's equation," *International Journal of Modern Physics C*, vol. 31, no. 9, 2020.

[25] W. M. Abd-Elhameed and Y. H. Youssri, "Connection formulae between generalized lucas polynomials and some Jacobi polynomials: application to certain types of fourth-order BVPs," *International Journal of Applied and Computational Mathematics*, vol. 6, no. 2, pp. 45–19, 2020.

[26] O. A. Abegunrin, S. O. Okhuevbie, and I. L. Animasaun, "Comparison between the flow of two non-Newtonian fluids over an upper horizontal surface of paraboloid of revolution: boundary layer analysis," *Alexandria Engineering Journal*, vol. 55, no. 3, pp. 1915–1929, 2016.

[27] A. F. Horadam, *Vieta Polynomials*, The University of New England, Armidaie, Australia, 2000.

[28] P. Agarwal and A. A. El-Sayed, "Vieta-Lucas polynomials for solving a fractional-order mathematical physics model," *Advances in Difference Equations*, vol. 2020, no. 1, pp. 1–18, 2020.

[29] M. Zakaria, M. M. Khader, I. Al-Dayel, and W. Al-Tayeb, "Solving fractional generalized fisher-Kolmogorov-Petrovsky-Piskunov's equation using compact finite different method together with spectral collocation algorithms," *Journal of Mathematics*, vol. 2022, Article ID 1901131, 9 pages, 2022.

[30] H. M. El-Hawary, M. S. Salim, and H. S. Hussien, "Ultraspherical integral method for optimal control problems governed by ordinary differential equations," *Journal of Global Optimization*, vol. 25, no. 3, pp. 283–303, 2003.